Automatic Luminal Contour and Calcification Detection in Intravascular Ultrasound Images

Esmeraldo dos Santos Filho[1], Yoshifumi Saijo[2], Makoto Yoshizawa[3] and Akira Tanaka[4]
1 Graduate School of Engineering, Tohoku University
2 Institute of Development, Aging and Cancer, Tohoku University
3 Information Synergy Center, Tohoku University
4 College of Symbiotic Systems Science, Fukushima University
esmeraldo@ieee.org

***Abstract*—Innovative applications of image processing techniques for analysis of intravascular ultrasound images are presented. This work has two main objectives: (1) to detect the luminal contour which is necessary to assess the degree of vessel stenosis, and (2) to detect presence of calcification, which is an important information for definition of the intervention method. These problems were addressed using a combination of mathematical morphology techniques, fuzzy systems, and *a priori* knowledge of the problems. Encouraging results were found when the results were compared with images manually segmented by expert medical doctors.**

Keywords: ultrasound; texture; image segmentation

I. INTRODUCTION

The objective of this work is to develop a system for automatic segmentation of calcifications and luminal contour in intravascular ultrasound (IVUS) images as a tool to support coronary artery disease diagnosis.

Luminal contour segmentation is important because the lumen area can give the medical doctor information about the degree of vessel stenosis. On the other hand, the presence or absence of calcium demonstrated by IVUS has been shown to be an important determinant of the transcatheter intervention success.

However, in general, autonomous segmentation is one of the most difficult tasks in digital image processing. Segmentation accuracy determines the eventual success or failure of computerized analysis procedures.

In this paper, as in Brusseau's [1] and Bovenkamp's [2] works, we proposed a system for automatic luminal contour segmentation. Unlike the Brusseau's system, our system is applied on images obtained from a rotating IVUS system due to the fact that these systems are largely used in clinical settings. Instead of a multi-agent system, as proposed by Bovenkamp, we used a simpler and powerful set of features proposed by Tuceryan [3] to achieve our goal of luminal contour segmentation.

Our strategy to achieve this goal is to extract local moment based texture features and a proposed pixel position feature from IVUS images to perform clustering on the basis of these features.

This work was supported by Health and Labor Sciences Research Grants H15-Fiji-001 of Ministry of Health Labor and Welfare of Japan and the Grant of Tohoku University 21 COE Program: 'Future Medical Engineering based on Bio-nanotechnology'.

II. MATERIALS AND METHODS

In this work, we used a commercial available IVUS system (Clear View Ultra, Boston Scientific, USA). The central frequency of the rotating IVUS probe (Atlantis SR Pro, Boston Scientific, USA) was 40 MHz..

A. Moments

Our algorithm uses the moments of an image to compute texture features. The $(p+q)$-th order moment m_{pq} of a function of two variables $f(x,y)$ with respect to the origin (0,0) is defined as [3]:

$$m_{pq} = \int_{-\infty}^{\infty} \int_{-\infty}^{\infty} f(x,y) x^p y^q \, dxdy \qquad (1)$$

where $p,q = 0,1,2, \ldots$

In this paper, as in Tuceryan's work [3], we regard the intensity image as a function of two variables, $f(x,y)$. We compute a fixed number of the lower order moments for each pixel in the input image (we use $p+q \leq 2$). The moments are computed within a small local window around each pixel. Given a window size W, the coordinates are normalized to the range of [-0.5 , 0.5] and the pixel is located at the center. The moments are computed with respect to this normalized coordinate system. This permits us to compare the set of moments computed for each pixel.

Let (i,j) be the pixel coordinates for which the moments are computed. For a pixel with coordinates (k,l) which falls within the window, the normalized coordinates (x_k,y_l) are given by:

$$x_k = \frac{k-i}{W} \qquad y_l = \frac{l-j}{W} \qquad (2)$$

Then the moment $m_{pq}(i,j)$ within a window centered at pixel (i,j) is computed by a discrete sum approximation of Equation (1) that uses the normalized coordinates:

$$m_{pq} = \sum_{k=-W/2}^{W/2} \sum_{l=-W/2}^{W/2} f(i+k, j+l) x_k^p y_l^q \qquad (3)$$

This discrete computation of the set of moments for a given pixel over a finite rectangular window corresponds to a neighborhood operation, and, therefore, it can be interpreted as a convolution of the image with a mask [3].

The set of values for each moment over the entire image can be regarded as a feature image. Let M_k be the k-th such image. If we use n moments, then there will be n such moment images. In our experiments, we used up to second order moments. That is, we used m_{00}, m_{01}, m_{10}, m_{11}, m_{02}, m_{20} which result in the images, M_1, M_2, M_3, M_4, M_5, and M_6 respectively.

To enhance the discrimination power of these moments, we adopted the transformation used by Tuceryan [3]. Then, we introduced a nonlinear transformation that maps moments to texture features.

Thus, we obtain the texture feature image F_k corresponding to the moment image M_k with mean $\overline{M_k}$ using the following transformation:

$$F_k(i,j) = \frac{1}{L^2} \sum_{(a,b)\in\omega_{ij}} \left| \tanh\left(\sigma\left(M_k(a,b) - \overline{M_k}\right)\right) \right| \quad (4)$$

where: ω_{ij} is an $L \times L$ averaging window centered at location (i,j) and σ controls the shape of the function. The parameters (in Eq.4): σ, moment window size W, and average window size L were chosen by gradually adjusting these values and observing the resultant effect in the segmented images. The final chosen values were W=7, L=9 and $\sigma = 0.01$. They were determined empirically.

B. Luminal Contour Definition

Due to the encouraging results obtained by Tuceryan [3], the theory of moment based texture segmentation was applied to the problem of luminal contour detection in IVUS images. The system proposed in this paper is comprised by the following modules.

Input image. The input image is the original image obtained from the IVUS system described in the beginning of this section.

Feature extraction. The feature extraction module is in charge of extraction of the transformed versions of the moments, F_k; k=1, 2, ...,6, and the radial distance R presented graphically in Fig.1.

In this work, we define the radial distance R as the distance from the central pixel of the image and the position of the pixel P under consideration. This distance R is normalized and becomes the seventh feature used in the following clustering of the input image pixels. The radial distance R is of fundamental importance because it helps pixels that are at similar distance from the center of the image to be included in the same cluster if they have similar texture features. The effect of using these texture and position features is that the clusters become organized in regions similar to concentric rings around the central pixel. This is associated with physiological structure of the blood vessels as represented in Fig.1. Thus, these seven features are used to comprise a feature vector for each pixel of the image.

Clustering. Based on their feature vectors, the input image pixels were clustered in this module using the Fuzzy C Means algorithm [4]. The chosen number of clusters was four: one cluster for the region outside the vessel, one for the region between the adventitia and intima, one for the lumen and another one for the catheter zone.

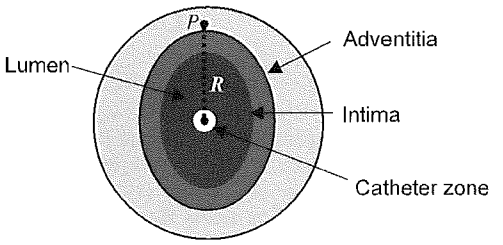

Fig.1 – Illustration of a cross section of a blood vessel

Morphological contour smoothing. In order to reduce the irregularities of the borders as well as some small regions around the borders, a morphological filtering is done prior to boundary detection. This filtering is performed through the application of opening and closing morphological operations with a disk structuring element of size 3.

Boundary detection. After the clustering and contour smoothing, the images had very well defined regions that could have their contour easily detected by traditional edge detection methods. In this system we used the Sobel operator due to its simplicity and efficiency.

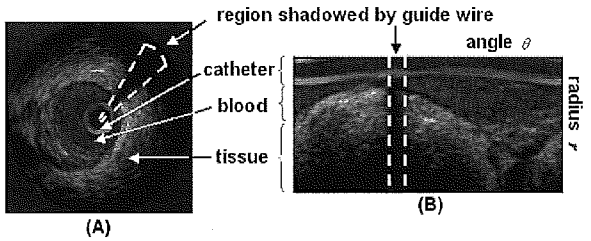

Fig.2 – Example of Cartesian coordinate system image (A) and its corresponding polar coordinate system version (B)

Output image. An example of the final output image can be observed in Fig.4(A).

C. The Guide Wire Shadow Problem

Sometimes due to the presence of the guide wire a region of the input image becomes shadowed and then contains no texture information. This may causes segmentation error. To solve this problem we proposed a contour correction procedure comprised of the following steps:

1) Convert the image with segmentation error from Cartesian coordinate system to polar coordinate system. An example of this process is shown in Fig.2.

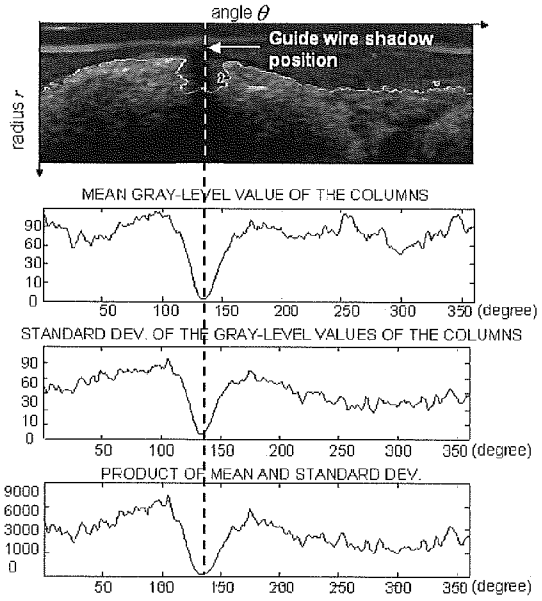

Fig.3 – Example of the search for the guide wire shadow position in polar coordinate system image based on the values of mean gray level and standard deviation of each column.

2) Automatically find the guide wire shadow. This step is carried out through the calculus of the mean gray-level and standard deviation of every column of the polar coordinate system converted image. The column which contains minimum value of the product of the mean gray-level by standard deviation is assumed to be the position of the guide wire shadowed region as illustrated in Fig.3. The catheter region was ignored during this process to avoid the influence of the ring-down artifact.

3) Erase the contour wrongly drawn in the guide wire shadow region and draw a new contour in the erased region through linear interpolation.

4) Convert the corrected image back to the Cartesian system.

RESULTS AND DISCUSSION I

Using the system presented above, tests were done with 15 *in vivo* coronary IVUS images from different patients. High correlation coefficients between the luminal contour automatically and the contour manually detected were found. These correlation coefficients values revealed preservation of standard deviation (0.92), mean gray level (0.89), and area (0.87) in the regions automatically segmented. An example of the results is shown in Fig.4 together with the image segmented by a medical doctor for comparison.

Our preliminary tests suggest that the moment based texture features together with the radial distance are feasible components for a feature vector in IVUS image segmentation when the aim is to find the luminal contour. A contour correction procedure based on the mean gray level and variance of each column of the polar coordinate version of the input image was presented as a feasible solution for the problem of error generated by the guide wire shadow.

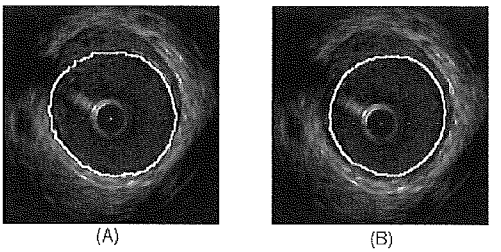

Fig.4 – Example of luminal contour detection. (A) and (B) are the same images obtained from patient A. (A) Automatically defined contour. (B) manually defined contour

IV CALCIFICATION DETECTION

One of the characteristics of the calcification regions is that they usually present high intensity echo for IVUS images. This fact makes it possible to segment calcified regions by gray level threshold techniques. However as the intensity level change from image to image it is quite difficult to find a single threshold level that could provide an accurate segmentation for a large group of images. Thus, it is necessary to adapt the threshold level to every single image.

A. Adaptive Threshold Estimator

Otsu [5] developed an optimal threshold selection method based on the maximization of the separability of the resultant classes. Thus, due to its simplicity and efficiency Otsu's method was used as threshold estimator in this segmentation algorithm.

The process of threshold selection presented is iteratively used to automatically generate threshold values for multiscale segmentation. For such automatic process, the following algorithm was implemented:

Step 1: Compute the histogram.

Step 2: Compute the optimal threshold.

Step 3: Compute a new histogram for the image with gray levels greater than the threshold.

Step 4: Go to step 2

After perform several tests, it was observed that two iterations of the above algorithm were sufficient to obtain an approximate segmentation of the regions of calcification that will be considered region of interest (ROI).

B. Identification of Calcification from the ROIs

Together with the intensity, another characteristic of the calcification regions is that they are usually followed be an acoustic shadow due to the strong reflection of the ultrasound bean in these regions.

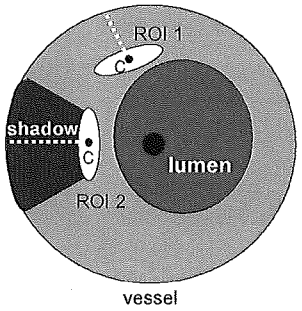

Fig.5 – Example of identification of calcification acoustic shadow .

Thus an efficient way to decide whether a given ROI is a calcification region or not is through analysis of the region posterior to this ROI. As shown in Fig.5.

We can observe in Fig.5 that the region of calcification (ROI 2) is followed by an acoustic shadow and then will present a level for median of the gray level values (in the dotted line) lower then the one of ROI 1.

Thus, in order to detect the acoustic shadow and then determine whether a given ROI is calcification or not, the following algorithm was constructed:

Step 1: Determine the centroid *C* of the ROI.

Step 2: From the centroid of the ROI to the outer boundary of the image, calculate the median gray level value *Med*.

Step 3: If $Med \leq T_{med}$ than classify the ROI as calcification. Else, classify ROI as non-calcification

T_{med} was chosen based on tests with several images.

V RESULT AND DISCUSSIONS II

Using the algorithms for adaptive thresholding and acoustic shadow detection tests were done. Varying the threshold T_{med} in the range from 80 to 210 and observing the number of true positive and false positive, a receiver operating characteristic (ROC) curve was constructed. It is shown in Fig.6. The area under the curve (AUC) is equal to 0.87. For the chosen T_{med}=130 the rate of true positive was 84% and the rate false positive was 12%. Thus, we had sensitivity = 0.84 and specificity = 0.88.

VI CONCLUSIONS

Otsu's algorithm for threshold selection has been successfully applied for segmentation of calcification regions

in IVUS images. However, some bright regions of normal tissue are also, often, segmented. Then an algorithm for identification of the ROIs that are really regions of calcification was implemented taking as identification criteria the presence or absence of acoustic shadow. A ROC curve was plotted showing the performance of the proposed algorithm.

A moment based texture feature together with a position feature presented encouraging results in luminal contour detection . As future works we plan to expand the algorithms for detection of vessel contour and other kind of plaques.

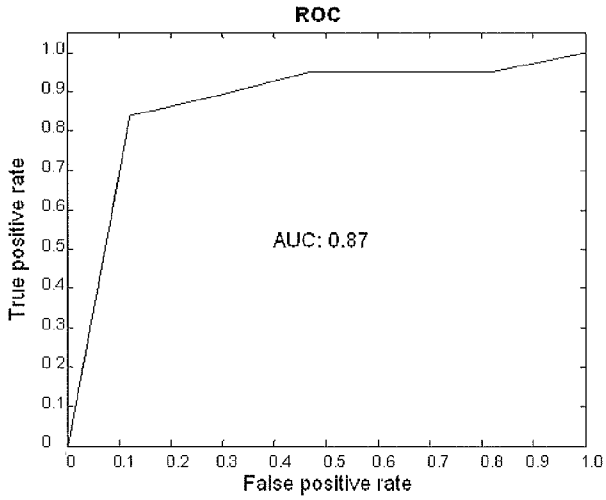

Fig.6 – Receiver Operating Characteristic (ROC) curve.

REFERENCES

[1] E. Brusseau *et al*, Fully automatic luminal contour segmentation in intracoronary ultrasound imaging – a statistical approach, IEEE Trans. on Medical Imaging, Vol. 23, No. 5, pp.554-566, May 2004

[2] E.G.P. Bovenkamp *at al*, Multi-agent segmentation of IVUS images, Pattern Recognition, Elsevier, Vol. 37, pp. 647-663, No. 4, April 2004.

[3] M. Tuceryan, Moment based texture segmentation, Proceedings of 11th IAPR International Conference on Image, Speech, Signal Analysis and Pattern Recognition, pp.45-48, 1992

[4] J.C. Bezdek, Pattern recognition with fuzzy objective function algorithms, Plenum Press, New York, 1981

[5] N. Otsu, A threshold selection method from gray-level histograms, IEEE Trans. on Systems, Man, and Cybernetics, smc-9, pp.62-66, 1979.

Elasticity Imaging of Artery Wall for Transcutaneous Tissue Characterization

Hideyuki Hasegawa, Jun Inagaki, Hiroshi Kanai, Masataka Ichiki[1], and Fumiaki Tezuka[2]
Department of Electronic Engineering,
Graduate School of Engineering, Tohoku University
Sendai 980-8579, Japan
hasegawa@us.ecei.tohoku.ac.jp
[1] Sendai Hospital of East Railway Company, Sendai 983-8520, Japan
[2] Sendai Medical Center, Sendai 980-0022, Japan

***Abstract*—This paper describes a noninvasive method for evaluating regional elasticity of atheroma by measuring the minute change in thickness of the arterial wall during one heartbeat. By comparing the pathological findings with the elasticity images, elasticity distributions for lipid and fibrous tissue (mixture of smooth muscle and collagen fiber) were determined *in vitro*. Furthermore, to characterize the fibrous cap of plaque, which almost consists of smooth muscle and collagen fiber, the correlation between the collagen content and elasticity was investigated for fibrous tissue. Based on these elasticity reference data, fibrous tissue surrounding the soft inclusion of lipids was noninvasively clarified in a carotid plaque and the collagen content in the fibrous cap was also estimated. This method offers potential for detection of plaque vulnerability in a clinical setting.**

Keywords-Small change in thickness of artery wall; Elasticity imaging; Atherosclerosis

I. INTRODUCTION

Rupture of atherosclerotic plaque is probably the most important factor underlying the sudden onset of the acute coronary syndrome [1]. Direct characterization of the composition and vulnerability of atherosclerotic plaque, rather than of the angiographic lumen [2], may offer insight into the mechanisms of plaque regression and progression [3] and thereby promote evaluation of cholesterol-lowering therapy [4] for reduction of cardiovascular events. MRI and intravascular ultrasound are promising technologies for directly imaging plaque morphology [5]. For the evaluation of dynamic mechanics, arterial elasticity has been determined by measuring the rough change in the diameter of the artery [6]. However, a method to detect the vulnerability of atherosclerotic plaque with sufficient accuracy has not yet been reported. The purpose of this study was to measure cross-sectional elasticity images in arterial walls with transcutaneous ultrasound.

II. MATERIALS AND METHODS

A. *In vitro experimental setup*

Figure 1 shows the experimental setup for *in vitro* experiments using excised human femoral arteries. The change in internal pressure was generated using an artificial heart, and the internal pressure was measured with the pressure catheter (Camino 110-4) placed in the lumen of the artery. The artery fixed in the water tank was measured with a linear probe (center frequency: 7.5MHz).

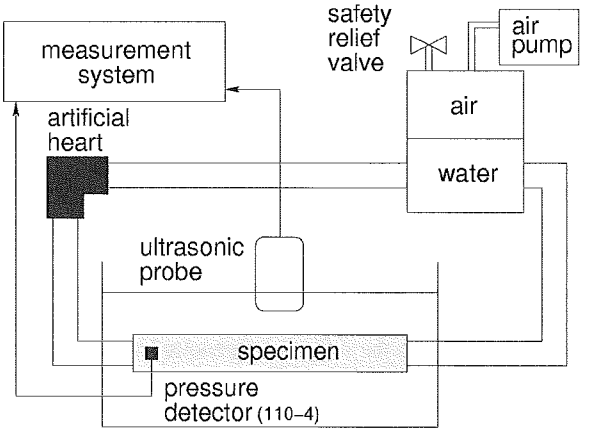

Figure 1: Experimental setup.

B. *Elasticity estimation* [7-9]

An ultrasonic beam was sequentially scanned at M (=60) positions with a linear-type ultrasonic probe of 7.5 MHz using conventional ultrasound diagnostic equipment (Toshiba SSH-140A), and multiple (N_m+1) points were preset from the luminal surface to the adventitia along the m-th ultrasonic beam (m=1,..., M) with constant intervals of h_0=375 μm at a time t_0 just before the ejection period. By dividing the arterial wall into multiple layers, we defined the n-th layer (n=1,..., N_m) as being between two contiguous points, n and n+1, along each beam. For measurement of change in thickness of each of the N_m layers, the instantaneous depth $x_{m,n}(t)$ of the n-th point along the m-th beam was simultaneously tracked by applying the *phased tracking method* to the received ultrasound. The minute decrease of several tens of micrometers in wall thickness of the n-th layer resulting from the arrival of the pressure wave at the beginning of the ejection period was determined by $\Delta h_{m,n}(t)=x_{m,n+1}(t)-x_{m,n}(t)-h_0$.

In the *phased tracking method*, for calculation of the auto-correlation function between the quadrature demodulated signals of sequentially received echoes, minute phase change of about 0.4 degrees caused by movement of the n-th point during the pulse transmission interval ΔT (=200 μs) can be accurately determined by introducing a constraint, namely, that their waveforms are identical but their phase values change. The lowest value of the change in thickness was validated as being about 0.5 μm by expanding a rubber plate in a water tank. Such a minute change in thickness cannot be measured by any other method. From the ratio of the maximum decrease in thickness during one heartbeat, $\Delta h_{m,n,\max}=\max_t|\Delta h_{m,n}(t)|$, to the initial thickness h_0 of the n-th layer, the maximum deformation of the n-th layer was obtained by $\Delta\varepsilon_{m,n,\max}=\Delta h_{m,n,\max}/h_0$. Since the deformation was sufficiently small and was in the linear regime, it showed incremental strain in the radial direction. By assuming that the arterial wall is incompressible and that the blood pressure is applied normal to each layer, the elastic modulus of the n-th layer along the m-th beam, $E_{\theta,m,n}$, is approximately given by [9]

$$E_{\theta,m,n} \cong \frac{1}{2}\left(\frac{\rho_{m,n,0}}{h_0 \cdot N_m} + \frac{N_m - n + 1}{N_m}\right)\frac{\Delta p}{\Delta \varepsilon_{m,n,\max}}, \quad (n=1,\ldots,N_m;\ m=1,\ldots,M) \tag{1}$$

where $\rho_{m,n,0}$ is the initial inner radius of the curvature of the n-th layer along the m-th beam at a time t_0. We assumed that the pressure in the arterial wall decreases linearly with the distance from the intimal side to the adventitia and that the arterial wall is almost isotropic.

For the region with a length of 18 mm along the axis of the artery, the regional elasticity $E_{\theta,m,n}$ was estimated on the cross-sectional image. Since the reflected ultrasound was received at a sampling interval of 100 ns (=75 μm along depth direction) after the quadrature demodulation, we further divided each layer with a thickness of h_0 into 5 points, shifted the initial depth of each layer by 1/5 of h_0 and applied the above procedure to each depth. Thus, $E_{\theta,m,n}$ was estimated at intervals of 75 μm in the depth direction and 300 μm in the axial direction. Using a silicone rubber tube with two layers set in an artificial circulation system, the accuracy of the measurement of regional elasticity for each layer has already been validated to be about 0.1 MPa, that is, the error is about 8% of the elasticity value obtained by a separate static pressure-diameter test.

C. *Construction of elasticity distribution* [8]

In this study, the elasticity distributions were obtained with respect to fibrous tissue (mixture of smooth muscle and collagen) and lipids. After ultrasonic elasticity measurements, the arteries were fixed in formalin. The plane scanned by ultrasound was identified by imaging a needle, which was fixed in the external surface of the posterior wall, in the B-mode image during the ultrasonic measurement. The pathological images of the measured planes were made with elastica-masson staining. By referring to the pathological images, the regions which correspond to fibrous tissue and lipids were assigned in the corresponding cross-sectional elasticity images. From the regions assigned for respective tissues, elasticity distributions were determined.

D. *Analysis of correlation between collagen content and elasticity* [10]

Fibrous tissue consists mainly of collagen fibers and smooth muscle. The correlation between the collagen content and the elasticity was investigated with respect to fibrous tissue to noninvasively estimate the collagen and smooth muscle contents based on the measured elasticity. In the elasticity image, there are M ultrasonic beams and N_m regions along m-th beam (m=1, 2,..., M). Therefore, in an elasticity image, there are $\sum_{m=1}^{M} N_m$ regions with respective elasticity values. Each region in an elasticity image is referred as $R^E_{m,n}$ (m=1, 2,..., M; n=1, 2,..., N_m). As shown in Fig. 2, each region $R^E_{m,n}$ in the elasticity image is compared with the corresponding region $R^P_{m,n}$ in the pathological image assigned as follows: The entire pathological image, which corresponds to the entire elasticity image, is divided into M sections in the axial direction of the artery, and each m-th section of M sections is divided into N_m regions in the radial direction. The sizes of all regions in an elasticity image are equivalent. However, actual sizes of regions assigned in the pathological image differed because of the distortion of the arterial wall due to dehydration during formalin fixation. In this study, by assuming that the change in size due to distortion is homogeneous, each M section was divided into N_m regions of equivalent size in the radial and axial directions. Then, the collagen content of each region $R^P_{m,n}$ assigned in the pathological image was estimated using the Mahalanobis distance. In this study, the composition of each region $R^P_{m,n}$ is classified into one of four classes (i=1: collagen, 2: smooth muscle, 3: elastin, 4: background). The mean, $\boldsymbol{\mu}=(\mu_r, \mu_g, \mu_b)^T$, and covariance matrix, Σ_i, of RGB values were determined for each class i by manually assigning typical regions in the pathological image for each class. From the determined mean $\boldsymbol{\mu}_i$ and the covariance matrix Σ_i, the Mahalanobis distance d_i^2 between each pixel, $\boldsymbol{X}=(x_r, x_g, x_b)^T$, in the region $R^P_{m,n}$ and the center of the i-th class is obtained as follows:

$$d_i^2 = (X-\mu_i)^T \Sigma_i^{-1} (X-\mu_i). \tag{2}$$

Each pixel $\boldsymbol{X}$ is classified into class $i_{\min}$ which has the least Mahalanobis distance to $\boldsymbol{X}$. To evaluate the collagen content in fibrous tissue, we employed two arteries mainly consisting of fibrous tissue. In the process for creating the pathological image, some deformations unavoidably occur. Such deformations lead to differences in size and shape between the elasticity and pathological images. Therefore, we used a part of the arterial wall showing little differences in size and shape between the elasticity and the pathological images.

The resolution was too small to exactly correlate a region in the elasticity image to the corresponding region in the pathological image because of the deformation caused by dehydration. Therefore, we employed spatially averaged values

obtained from regions of 0.6 mm in the axial direction and 0.6 mm in the radial direction in size.

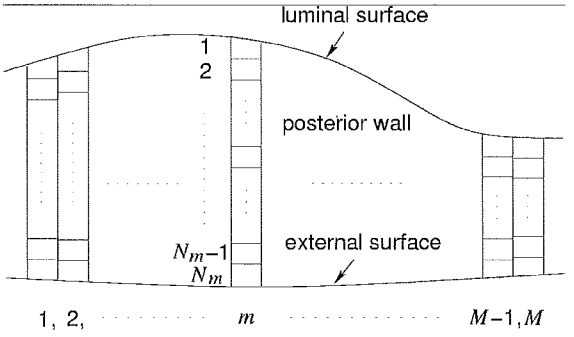

Figure 2: Illustration of assigning small regions in elasticity and pathological images.

III. Results

A. Elasticity distributions of lipids and fibrous tissue

Figure 3(1) shows two typical elasticity images of iliac arteries measured *in vitro*. Figure 3(2) shows pathological images of the corresponding sections. By referring to pathological images, lipids and fibrous tissue (mixture of smooth muscle and collagen) were determined as shown in Fig. 3(2), and the corresponding regions were assigned in elasticity images as shown in Fig. 3(1). Figure 3(3) show elasticity distributions of respective assigned regions. By applying the same procedure to nine arteries, mean and standard deviation in elasticity were determined to be 81±40 kPa and 1.0±0.63 MPa for lipids and fibrous tissue, respectively (Fig. 3(4)).

B. Collagen contents vs. elasticity

Pathological images shown in Fig. 4(b) were divided into small regions which correspond to the resolution of elasticity images (Fig. 4(a)). Figure 5 shows the relationship between the collagen content and elasticity. Plots and vertical bars show spatial mean and standard deviation in each 600 μm×600 μm region. Positive correlation was found in Fig. 5 and the regression line was estimated by the least-squares method. Figure 6 shows the relationship between smooth muscle and collagen contents in each small region in pathological images, and fibrous tissue is found to almost consist of smooth muscle and collagen. Therefore, both collagen and smooth muscle contents in fibrous tissue are estimated using the regression line in Fig. 5.

C. In vivo tissue characterization

Based on the elasticity reference data determined by *in vitro* experiments, an elasticity image (Fig. 7(a)), which was noninvasively measured *in vivo*, was classified as one of three categories (lipid, fibrous tissue, or other). In Fig. 7(b), regions classified as lipids and fibrous tissue were colored by yellow and cyan, respectively. Furthermore, smooth muscle and collagen contents in fibrous tissue were estimated as shown in Fig. 7(c).

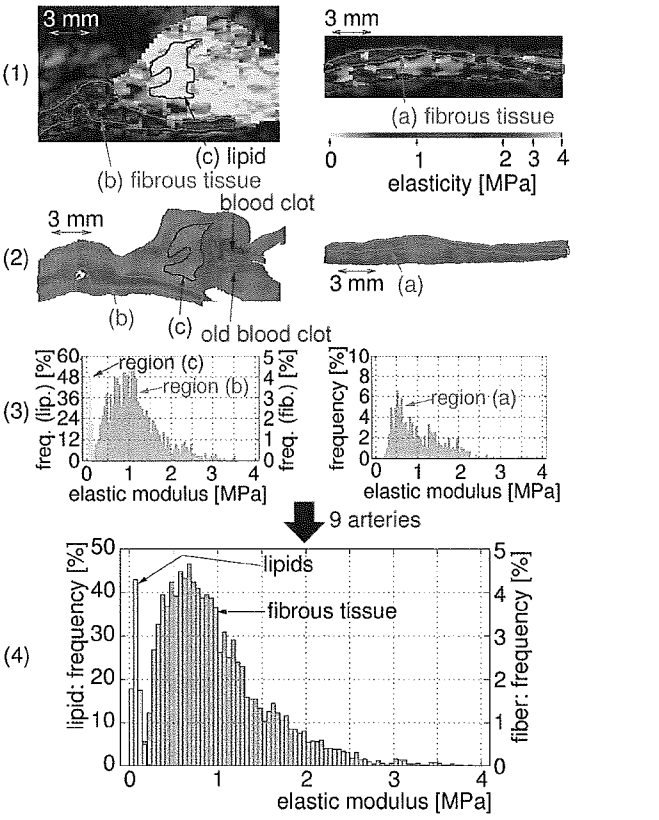

Figure 3: (1) Elasticity images of extracted iliac arteries. (2) Pathological images of corresponding sections. (3) Elasticity distributions for respective assigned regions shown in (1). (4) Elasticity distributions for lipids and fibrous tissue obtained from 9 arteries.

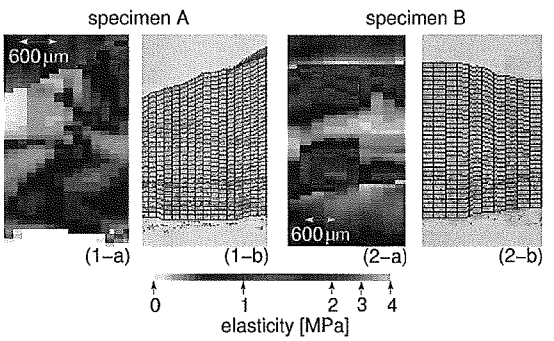

Figure 4: (a) Elasticity images. (b) Corresponding pathological images.

IV. Conclusion

Cross-sectional images of the elasticity around atherosclerotic plaque were transcutaneously measured in this study. By comparing the elasticity and pathological images, elasticity distributions of lipids and fibrous tissue were determined as the 'elasticity library'. Using the elasticity library, the elasticity image measured with transcutaneous

ultrasound was classified into lipids and fibrous tissue. Furthermore, a positive correlation was found in the relationship between elasticity and the collagen content in fibrous tissue, and these results offer a potential for estimating collagen content in the classified fibrous tissue. The proposed novel approach has a potential for non-invasive tissue characterization and diagnosis of the vulnerability of plaque in a clinical setting.

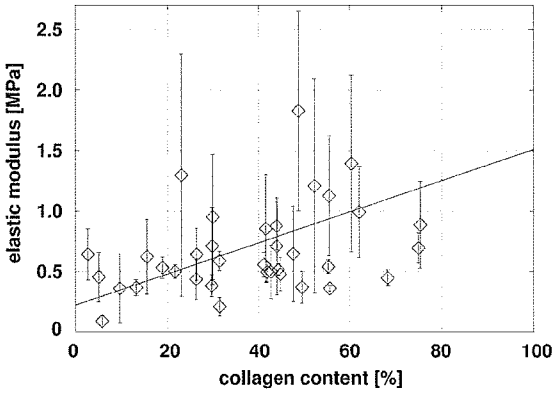

Figure 5: Relationship between the collagen content and elasticity.

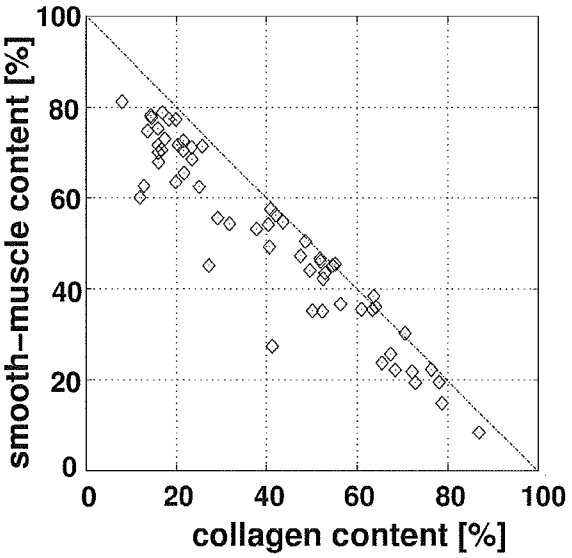

Figure 6: Relationship between smooth muscle and collagen contents in each small region in pathological images shown in Fig. 4(b).

References

[1] P. R. Moreno, E. Falk, I. F. Palacios, J. B. Newell, V. Fuster, and J. T. Fallon, "Macrophage infiltration in acute coronary syndromes. Implication for plaque rupture," Circulation, vol. 90, pp. 775-778, 1994.

[2] W. C. Little, M. Constantinescu, R. J. Applegat, M. A. Kutcher, M. T. Burrows, F. R. Kahl, and W. P. Santamore, "Can coronary angiography predict the site of a subsequent myocardial infarction in patients with mild-to-moderate coronary artery disease?," Circulation, vol. 78, pp. 1157-1166, 1988.

[3] H. M. Loree, R. D. Kamm, R. G. Stringfellow, and R. T. Lee, "Effects of fibrous cap thickness on peak circumferential stress in model atherosclerotic vessels," Circ. Res., vol. 71, pp. 850-858, 1992.

[4] G. Brown, J. J. Albers, L. D. Fisher, S. M. Shaefer, J. T. Lin, C. Kaplan, X. Q. Zhao, B. D. Bisson, V. F. Fitzpatrick, and H. T. Dodge, "Regression of coronary artery disease as a result of intensive lipid-lowering therapy in men with high levels of apolipoprotein B," N. Engl. J. Med., vol. 323, pp. 1289-1298, 1990.

[5] B. N. Potkin, A. L. Bartorelli, J. M. Gessert, R. F. Newville, Y. Almagor, W. C. Roberts, and M. B. Leon, "Coronary artery imaging with intravascular high-frequency ultrasound," Circulation, vol. 81, pp. 1575-1585, 1990.

[6] F. Hansen, P. Mangell, B. Sonesson, and T. Länne, "Diameter and compliance in the human common carotid artery -variations with age and sex," Ultrasound Med. Biol., vol. 21, pp. 1-9, 1995.

[7] H. Kanai, M. Sato, Y. Koiwa, and N. Chubachi, "Transcutaneous measurement and spectrum analysis of heart wall vibrations," IEEE Trans. Ultrason. Ferroelect. Freq. Contr., vol. 43, pp. 791-810, 1996.

[8] H. Kanai, H. Hasegawa, M. Ichiki, and F. Tezuka, "Elasticity imaging of atheroma with transcutaneous ultrasound," Circulation, vol. 108, pp. 3018-3021, 2003.

[9] H. Hasegawa, H. Kanai, N. Hoshimiya, and Y. Koiwa, "Evaluating the regional rlastic modulus of a cylindrical shell with nonuniform wall thickness," J. Med. Ultrason., vol. 31, pp. 81-90, 2004.

[10] J. Inagaki, H. Hasegawa, H. Kanai, M. Ichiki, and F. Tezuka, "Construction of reference data for tissue characterization of arterial wall based on elasticity images," Jpn. J. Appl. Phys., vol. 44, pp. 4593-4597, 2005.

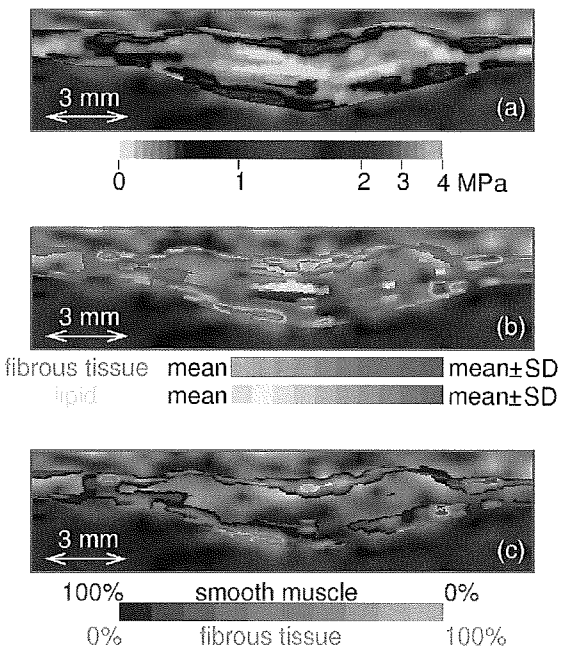

Figure 7: (a) Elasticity image of a carotid plaque of 71-year-old male with hyperlipidemia. (b) Detected fibrous tissue and lipids. (c) Estimated smooth muscle and collagen contents of fibrous cap.

Ultrasonic Measurement of Displacement Inside Object Caused by Dual Acoustic Radiation Force

Mikito Takahashi, Hideyuki Hasegawa, and Hiroshi Kanai
Department of Electronic Engineering
Graduate School of Engineering, Tohoku University
Sendai 980-8579, Japan
hkanai@us.ecei.tohoku.ac.jp

Abstract—**There are many studies on measurement of tissue mechanical properties by applying an acoustic radiation force induced by ultrasound to an object. However, when the elastic modulus of the object is much higher than that of the surrounding tissue (such like a tumor in the breast tissue), an acoustic radiation force might generate only the change in position of the object and the strain of the object is hardly generated. In such cases, mechanical properties of the object cannot be evaluated. In this study, two cyclic acoustic radiation forces are simultaneously applied to an object to effectively generate the strain inside the object even when the object is much harder than the surrounding tissue.**

Keywords-strain, dual acoustic radiation force

I. INTRODUCTION

This In recent years, some remote actuation methods based on acoustic radiation force have been reported. Fatemi and coworkers proposed an imaging method called ultrasound-stimulated acoustic emission (USAE) [1,2]. Their system consists of two confocal ultrasonic transducers, and two ultrasound beams with two slightly different frequencies of f and $(f+\Delta f)$ are transmitted. Acoustic radiation pressure, $P_R(t)$, exerted on the interface between two different media is a function of the energy density, $e(t)$, and the specific acoustic impedances, Z_1 and Z_2, of the media [3]. The energy density, $e(t)$, is proportional to the square of the sum of the sound pressures, $p_1(t)$ and $p_2(t)$, generated by the two transducers. In the intersectional area of the two beams, therefore, an oscillatory radiation pressure $P_R(t)$ with the frequency difference, Δf, is applied to the interface. The radiation force produces acoustic emission which is closely related to the mechanical frequency response of the medium. By measuring the acoustic emission with a hydrophone, hard inclusions in a soft material were experimentally detected. The spatial resolution in the depth direction corresponds to the size of the intersectional area.

Nightingale *et al.* proposed an alternative imaging method in which the pulsed ultrasound is employed for applying the radiation force to a soft tissue during short durations (less than 1 ms). The viscoelastic properties of the tissue are measured from the magnitude and the transient response of the displacement, $d(t)$, of the tissue [4]. In order to generate measurable displacement, $d(t)$, by several ultrasonic pulses, high-intensity pulsed ultrasound of 1,000 W/cm^2 is employed. According to the safety guideline shown by the Japan society of ultrasonics in medicine (JSUM), however, the intensity of ultrasound is recommended to be less than 240 mW/cm^2 and 1 W/cm^2, for the pulsed and continuous waves, respectively [5]. Therefore, the intensity of the pulsed ultrasound employed by Nightingale *et al.* is far greater than that indicated in the safety guideline.

To improve the spatial resolution, Michishita *et al.* used ultrasound correlation-based method, the ultrasonic phased tracking method [6], to measure the minute displacement, $d(t)$, caused by acoustic radiation force. Moreover, to suppress the sound pressure of the employed ultrasound, a continuous-wave (CW) ultrasound, which consists of the sum of frequency components of f and $f+\Delta f$, was employed to cyclically actuate the acoustic radiation pressure, $P_R(t)$, at low frequency f to increase the signal-to-noise ratio in displacement estimation [7].

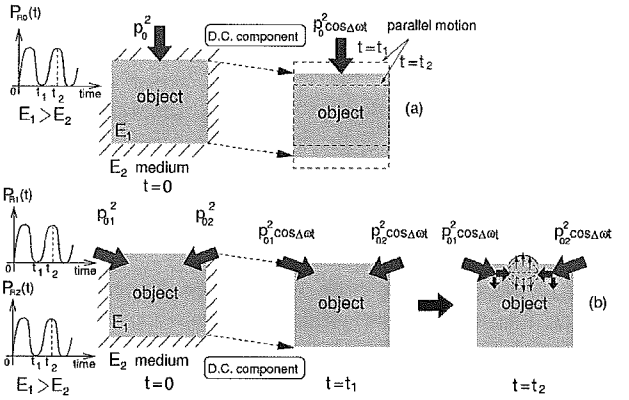

Figure 1: (a) Illustration of the change in position of an object caused by an acoustic radiation force. (b) Illustration of a strain of an object caused by two acoustic radiation forces.

However, as illustrated in Fig. 1(a), when the elastic modulus of the object is far greater than that of the surrounding media, an acoustic radiation force may generate only the change in position of the object. In such cases, the mechanical properties of the object cannot be estimated. In this paper, to generate the strain of the object even in such cases, two acoustic radiation forces with phases of ϕ and $\varphi+\Delta\varphi$ were applied at two different positions in the object as shown in Fig.

1(b). Furthermore, the displacements of the region inside the object, where the two acoustic radiation forces were applied, were measured by the ultrasonic *phased tracking method.*

II. Principle

When a continuous plane-wave ultrasound is incident on an interface between two different media, a constant force, which is called an acoustic radiation force, is exerted on the interface. Acoustic radiation pressure, $P_R(t)$, is defined as the acoustic radiation force per unit area of the interface as follows:

$$P_R(t)=(1+R^2)\,e(t) \tag{1}$$

where R and $e(t)$ are the reflection coefficient of sound pressure and the energy density at the interface, respectively. In eq. (1), the transmitted wave is assumed to be perfectly absorbed in the object. Using the densities, ρ_1 and ρ_2, and sound speeds, c_1 and c_2, of the media and object, the reflection coefficient, R, and the energy density, $e(t)$, are defined by

$$R=\frac{Z_2-Z_1}{Z_2+Z_1}=\frac{\rho_2 c_2-\rho_1 c_1}{\rho_2 c_2+\rho_1 c_1} \tag{2}$$

$$e(t)=\frac{1}{\rho_1 c_1^2}\,p^2(t) \tag{3}$$

where $p(t)$ is the sound pressure at the interface. The Japan society of ultrasonics in medicine (JSUM) shows the safety guideline, in which the intensity of the CW ultrasound should be less than 1 W/cm^2. By assuming that density ρ_1 and sound speed c_1 of water are 10^3 kg/m^3 and 1,500 m/s, respectively, the acoustic radiation pressure, $P_R(t)$, exerted on the interface of the totally absorbing object (R=0) is calculated to be 6.67 Pa when the ultrasound intensity is 1 W/cm^2.

The energy density, $e(t)$, of the incident wave is proportional to the square of the sound pressure, $p(t)$, of the ultrasound beam. When two ultrasonic beams with slightly different frequencies, f and $f+\triangle f$, are crossed each other, the sound pressure, $p_{sum}(t)$, at the intersectional area is expressed by the sum of sound pressures of two ultrasonic beams as follows:

$$p_{sum}(t)=p_0\cos\omega t+p_0\cos(\omega+\triangle\omega)t \tag{4}$$

where p_0, ω, and $\triangle\omega$ are the amplitude of the sound pressure of each ultrasound beam, angular frequency of the incident wave ($\omega=2\pi f$), and difference in angular frequency ($\triangle\omega=2\pi f$), respectively. For this case, the energy density, $e(t)$, is given by

$$\begin{aligned} e(t)&=\frac{\{p_{sum}(t)\}^2}{\rho_1 c_1^2}=\frac{p_0^2}{\rho_1 c_1^2}\{\cos\omega t+\cos(\omega+\Delta\omega)t\}^2 \\ &=\frac{p_0^2}{\rho_1 c_1^2}\left\{1+\cos\Delta\omega t+\cos(2\omega+\Delta\omega)t+\frac{1}{2}\cos 2\omega t\right. \\ &\quad\left.\frac{1}{2}\cos 2(\omega+\Delta\omega)t\right\} \end{aligned} \tag{5}$$

From the second term of the right-hand side of eq. (5), it is found that the energy density, $e(t)$, of the incident field has a component with the frequency difference $\triangle f$. Therefore, the cyclically oscillating radiation pressure, $P_R(t)$, at the frequency difference $\triangle f$ is given by

$$P_R(t)=\left(1+R^2\right)\frac{p_0^2}{\rho_1 c_1^2}\left(1+\cos\Delta\omega t\right) \tag{6}$$

Thus, using an ultrasound beam generated by the sum of signals at the slightly different frequencies, f and $f+\triangle f$, the oscillatory radiation force can be cyclically applied to the focal area of the beam.

In this study, in order to generate the regional strain inside the object, we use two phase-controlled acoustic radiation pressures, $P_{R1}(t)$ and $P_{R2}(t)$, given by

$$P_{R1}(t)=\left(1+R^2\right)\frac{p_{01}^2}{\rho_1 c_1^2}\left(1+\cos\Delta\omega t\right), \tag{7}$$

$$P_{R2}(t)=\left(1+R^2\right)\frac{p_{02}^2}{\rho_1 c_1^2}\left\{1+\cos(\Delta\omega t+\Delta\phi)\right\}, \tag{8}$$

where $\triangle\varphi$ is the phase difference between $P_{R1}(t)$ and $P_{R2}(t)$.

These two acoustic radiation forces at $\triangle f$ Hz, whose phase difference is $\triangle\varphi$, are applied by setting focal points at the different sites inside the object, and the insonification angles are assigned to θ_1 and θ_2 for respective transducers.

III. Experimental Setup

Before An experimental setup is illustrated in Fig. 2. In order to measure the strain, we employed ultrasonic diagnostic equipment (Toshiba SSH-160A) with a sector-type probe (center frequency: 5 MHz). The equipment was modified to detect the minute strain of the object by the ultrasonic {\it phased tracking method}. An object made of gel (45 mm×45 mm×17 mm, containing carbon to obtain a sufficient scattering) was placed in a water tank as shown in Fig. 2. For the application of radiation pressures, $P_{R1}(t)$ and $P_{R2}(t)$, two concave ultrasonic transducers were employed. A concave ultrasonic transducer (Tokimec 1Z20I-PF50-C; center frequency: 1 MHz) was driven by a sum of two continuous waves (CWs) at two slightly different frequencies of 1 MHz and 1 MHz + 10 Hz. The resultant ultrasound beam was focused at 45 mm away from the surface of the transducer, and the focal point was set at a point, α, on the top of the object with a beam angle, θ_1, from the vertical axis of 22 degrees. Another concave transducer (Tokimec 1Z20I-PF50-C; center frequency: 1 MHz) was driven by a sum of CWs at 1 MHz and 1 MHz + 10 Hz with a phase difference, $\triangle\varphi$, of 0 degrees. The focal point, which is 45 mm away from the surface of the transducer, was set at a point, β, on the top of the object with a beam angle, θ_2, of 23 degrees. The distance between α and β was set at 6 mm.

In this study, the spatial distributions of displacement inside the object are measured with ultrasound. In the ultrasonic measurement, the CW ultrasound for actuation will interfere in the pulsed ultrasound for strain measurement. In order to avoid this interference, it is necessary to stop actuation during transmission and reception of the ultrasonic pulse for the

measurement. Therefore, we used an electrical switch to control the cessation of the CW ultrasound for actuation [7].

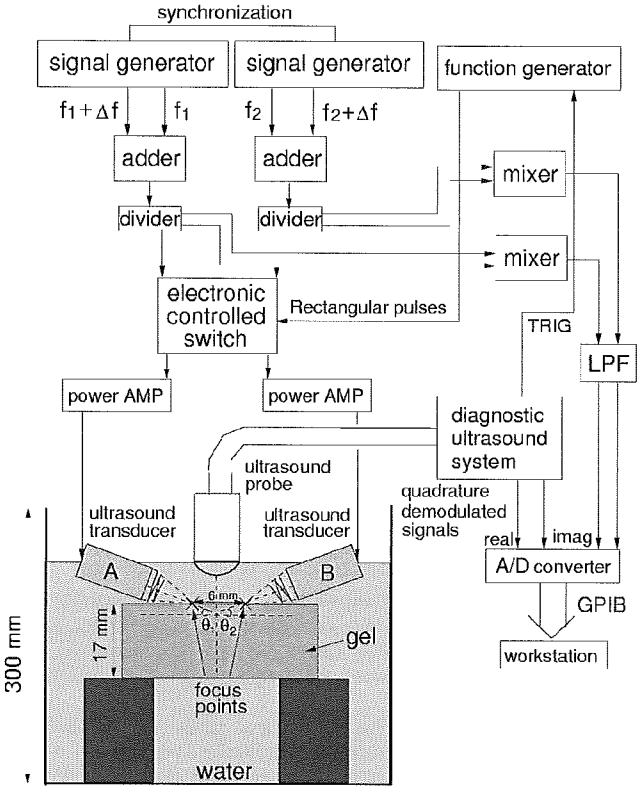

Figure 2: Experimental setup for measurement of the strain inside the object cyclically actuated using two concave ultrasonic transducers.

IV. Experimental Results

Figure 3(a) shows an M-mode image of the object. Acoustic radiation pressures, $P_{R1}(t)$ and $P_{R2}(t)$, shown in Figs. 3(b) and 3(c) were calculated based on eq. (6) as follows: The density, ρ_2, and the sound speed, c_2, of the object were measured as 1.1×10^3 kg/m^3 and 1.47×10^3 m/s, respectively, in a separate experiment. By assuming the density, ρ_1, and the sound speed, c_1, of water to be 1.0×10^3 kg/m^3 and 1.5×10^3 m/s, respectively, the pressure reflection coefficient, R, and the energy reflection coefficient, R^2, were respectively calculated as 0.038 and 0.0014 using eq. (2). In this paper, by assuming the object to be a totally absorbing material (R=0) and considering the angles, θ_1 and θ_2, of the transducer for the actuation from the vertical axis, the acoustic radiation pressures, $P_{R1}(t)$ and $P_{R2}(t)$, exerted on the two points in the object were calculated based on eq. (6). In this calculation, we obtained the amplitude of the focused sound pressures of p_{01} and p_{02} beforehand by measuring the acoustic fields of the each ultrasound for actuation with a hydrophone (Force Institute, MH-28-10).

The vibration velocity, $v(t)$, at a point in the object actuated by the acoustic radiation forces were measured by the ultrasonic *phased tracking method*, as shown in Fig. 3(d). By integrating the velocity, $v(t)$, the displacement, $d(t)$, of this point was obtained as shown in Fig. 3(e). In Fig. 3(e), it is found that the object was cyclically actuated at the frequency difference, $\triangle f$, of 10 Hz with an amplitude of the order of a few micrometers [7].

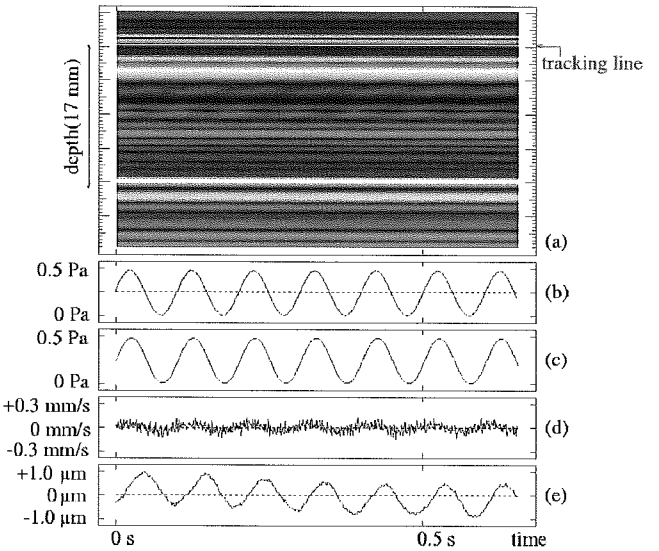

Figure 3: (a) M-mode image of a gel. (b) Acoustic radiation force, $P_{R1}(t)$. (c) Acoustic radiation force, $P_{R2}(t)$. (d) Velocity along the red line in (a). (e) Displacement obtained by integrating velocity in (d).

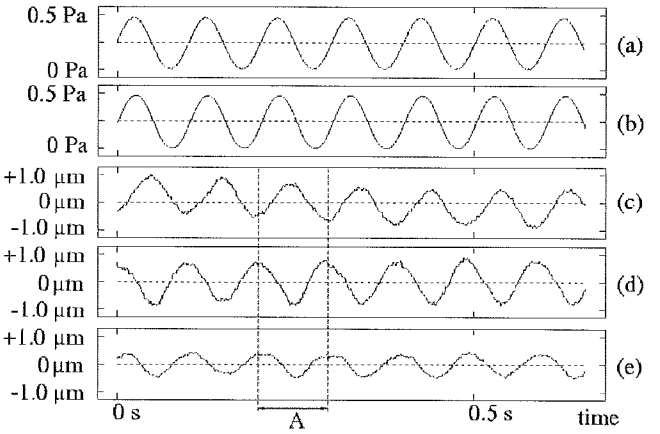

Figure 4: (a) Acoustic radiation force, $P_{R1}(t)$. (b) Acoustic radiation force, $P_{R2}(t)$. Displacements measured at (c) the surface of the gel, (d) a point 2.5 mm deeper than the surface, and (e) a point 3.0 mm deeper than the surface.

Two acoustic radiation forces were applied by setting focal points at the upper surface of the object. Angles, θ_1 and θ_2, of ultrasonic beams for actuation were set at 22 degree and 23 degree from the horizontal axis, respectively. Therefore, directions of horizontal components of the two acoustic radiation forces were opposite each other by setting $\triangle\varphi$=0. Therefore, the region between two focal points was cyclically compressed along the horizontal axis by these acoustic radiation forces, and the thickness of the region between two focal points becomes thick along the vertical axis.

Figure 4 shows displacements at multiple points along an ultrasonic beam. When acoustic radiation forces shown in Figs. 4(a) and 4(b) increase, the surface of the object moved upward. On the other hand, two points, which were 2.5 mm and 3.0 mm deeper than the surface, moved downward as shown in Fig. 4(d) and 4(e). This result show the thickness of the region between two focal points increased along the vertical axis.

Then, the 2-D displacement distribution was measured by moving the ultrasonic probe for the measurement in the horizontal direction as illustrated in Fig. 5(a). In Fig. 5(b), the directions and magnitude of measured displacements were shown by the direction and length of arrows. In Fig. 5(b), displacements relative to those at the beginning of the period A in Fig. 4 were shown at a time when acoustic radiation forces becomes maximum. From Fig. 5(b), it was found that the strain inside the object was successfully generated using two phase-controlled acoustic radiation forces.

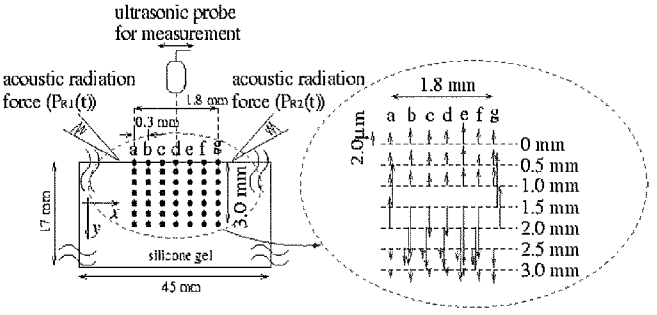

Figure 5: (a) Illustration of measuring 2-D spatial distribution of displacements inside the gel. (b) Measured 2-D spatial distribution of displacements inside the object.

V. Conclusion

The In this study, in order to generate the regional strain inside the object, we constructed an experimental setup for application of cyclic remote actuation in the object using two focused ultrasonic transducers. The phase difference between two acoustic radiation forces, which were respectively applied at two different positions in the object, was controlled to be 0 degrees. The resulting displacements inside the object were successfully measured by the ultrasonic *phased tracking method*. These results show potential of the proposed method for generation of the regional strain inside the object.

References

[1] M. Fatemi, and J. F. Greenleaf, "Vibro-Acoustic Mammography," IEEE Trans. Med. Imag., vol. 21, pp. 1-8, 2002.

[2] M. Fatemi, and J. F. Greenleaf, "Vibro-acoustgraphy: An imaging mdality based on ultrasound-stimulated acoustic emission," Proc. Nation. Acad. Sci. USA. vol. 96, pp. 6603-6608, 1999.

[3] G. R. Torr, ,"The acoustic radiation force," Am. J. Phys., vol. 52, pp. 402-408, 1984.

[4] K. Nightingale, M. S. Soo, R. Nightingale, and G. Trahey, "Acoustic radiation force impulse imaging: in vivo demonstration of clinical feasibility," Ultrasound Med. Biol., vol. 28, pp. 227-235, 2002.

[5] JSUM: Jpn. J. Med. Ultrason., vol. 11, p. 41, 1984 [in Japanese].

[6] H. Kanai, M. Sato, Y Koiwa, and N. Chubachi, "Transcutaneous Measurement and Spectrum Analysis of Heart Wall Vibrations," IEEE Trans. Ultrason., Ferroelect., and Freq. Contr., vol. 43, pp. 791-810, 1996.

[7] K. Michishita, H. Hasegawa and H. Kanai, "Ultrasonic Measurement of Minute Displacement of Object Cyclically Actuated by Acoustic Radiation Force," Jpn. J. Appl. Phys., vol. 42 pp. 4608-4612, 2003.

Noninvasive Measurement of Myocardial Viscoelasticity

Hiroshi Kanai
Department of Electronic Engineering
Tohoku University
Aramaki-aza-Aoba 6-6-05, Sendai 980-8579, Japan
E-Mail: kanai@ecei.tohoku.ac.jp

***Abstract*—This presentation proposes a novel method to noninvasively measure the myocardial viscoelasticity *in vivo* to evaluate the heart diastolic properties. By the ultrasonic measurement of the myocardial motion, we have already found that some pulsive waves are spontaneously excited by aortic-valve closure (AVC) at end-systole (T_0). In this study, a sparse sector scan at a sufficiently high frame rate clearly reveals *wave propagation* along the heart wall. The propagation time of the wave along the heart wall is very small, namely, *several milliseconds*, and cannot be measured by conventional equipment. From the measured phase velocity, we estimate the myocardial viscoelasticity *in vivo*. In *in vivo* experiments applied to 6 healthy subjects, the propagation of the pulsive wave was clearly visible in all subjects. For the frequency component up to 90 Hz, the typical propagation speed is about several m/s and rapidly decreased around the time of AVC. For the healthy subject, the typical value of elasticity was about 24-30 kPa and did not change around the time of AVC. The typical transient values of viscosity decreased rapidly from 400 Pa•s to 70 Pa•s around the time of AVC. The measured shear elasticity and viscosity in this study are comparable to those obtained for the human tissues using audio frequency in *in vitro* experiments reported in the literature. This method offers potential for *in vivo* imaging of the spatial distribution of the passive mechanical properties of the myocardium.**

Keywords: Phased tracking method, Viscoelasticity, Pulsive wave.

I. Introduction

Conventional ultrasonography, CT, and MRI enable clinical visualization of cross-sectional images of the human heart, but their imaging is restricted to large motion (> 1 mm) and low frequency components (< 30 Hz). The tissue Doppler imaging (TDI) technique enables determination of motion distribution of the myocardium in real time. Even in current measurement, however, the sampling frequency of the motion of the heart wall is low (at most 200 Hz [1]), that is, the sampling period is 5 ms, which is too long to detect the propagation time of the wave.

To measure the original vibrations of the heart sounds, we have already developed a method to transcutaneously measure the heart-wall vibrations as a waveform at one point or multiple points preset along an ultrasonic beam in the heart wall [2]. We found that there is a steep dip in the pulse which occurs exactly at the time of AVC (T_0) [3] as shown in **Fig. 1**. This *notch* has been also measured by the TDI approach to determine the time of AVC (T_0).

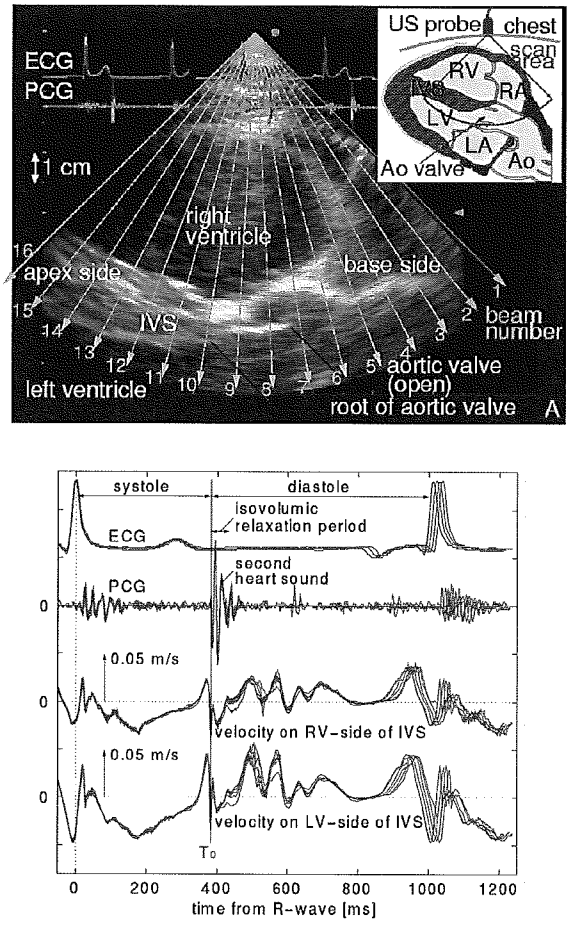

Figure 1. **upper:** A cross-sectional image measured by conventional echocardiography in a healthy young male (subject A). The arrows show the directions of the 16 ultrasonic beams used to measure the vibrations at about 160 points in the heart wall. **lower:** For the man at two points set along the 13th ultrasonic beam, each waveform for six consecutive cardiac cycles is overlaid.

As shown in the upper figure of **Fig. 1**, use of the sparse sector scan [3] has allowed us to simultaneously measure heart-wall motion at 160 points at a sufficiently high frame rate to measure the propagation of the *notch pulse* along the interventricular septum (IVS). From consecutively obtained spatial distributions of the phase value of the vibration wave, our study [4] has revealed for the first time that the steep dip of the notch pulse propagates along the IVS from the base to the apex, and its phase velocity is determined. By analyzing various frequency components up to 90 Hz, the propagation speed shows the frequency dispersion.

This study shows that this dispersion characteristic agrees with the theoretical one of the Lamb wave which propagates in the *viscoelastic plate immersed in fluid*. By introducing the single Voigt model into the equation of the Lamb wave and fitting the derived theoretical phase velocity to the measured dispersion, the myocardial viscoelastic properties are determined noninvasively for the first time.

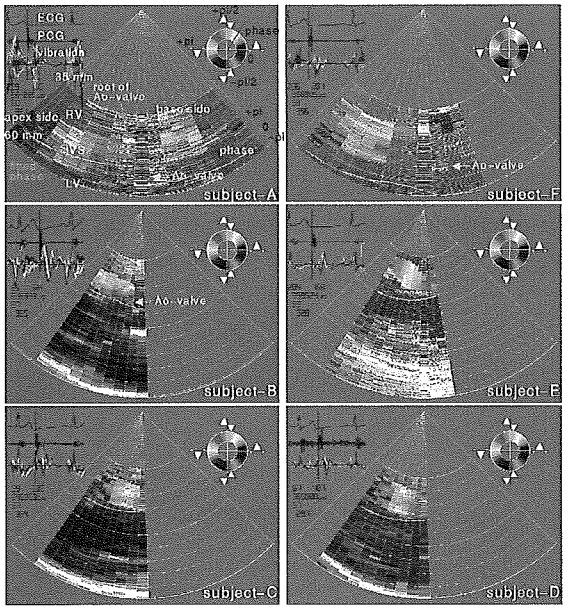

Figure 2. Spatial distributions of color-coded phase values for 60-Hz component of the notch pulse in **Fig. 1** for 6 healthy young subjects (A-F). The analyzed time corresponds to AVC (T_0).

II. Propagation of Pulsive Wave Along Heart Wall

Using a sparse sector scan in 16 directions, multiple points were preset at 770-μm intervals in the heart wall along each of 16 ultrasonic beams, and the vibrations at about 160 points were simultaneously measured as waveforms with a sampling frequency of 450 Hz by the phased tracking method [3].

Since the wavelength of the detected pulsive wave is about 100 mm for a 30-Hz component and is comparable to the size of the whole heart, its propagation phenomenon cannot be clearly visualized by showing the spatial distribution of the instantaneous *amplitude* of the pulsive wave. Therefore, using the method in [3], 2-D spatial distribution of the instantaneous *phase* values of the measured wave is shown in **Fig. 2**. For this imaging, the short time Fourier transform is applied to the pulsive wave at each point in **Fig. 1** after the pulsive wave is multiplied by the Hanning window with a short length of 35 ms. The phase value is detected for each frequency component from 10 Hz to 90 Hz, and then color-coded based on the upper-right circular figure. **Figure 2** shows the phase distributions for a 60-Hz component along the IVS at a time of AVC (T_0) for 6 healthy young subjects.

From the consecutively obtained cross-sectional 2-D images, a motion picture is presented. It can be seen that a few pulsive waves are radiated from the root of aortic valve and propagate along the IVS. The delay due to the propagation of the pulse from the root to the apex is several milliseconds, which has not been recognized at all by any other clinical technique.

III. Estimation of Viscoelasticity Using Lamb Wave and Voigt Models

To determine the instantaneous phase velocity of the pulsive wave, if the straight line with a constant gradient k [rad/m] is spatially fit to the instantaneous spatial distribution of the measured phase in each cross-sectional image in **Fig. 2**, the instantaneous phase velocity for the frequency component f_0 is determined by $2\pi f_0/k$. However, since there is initially some spatial distribution of the phase which is independent of the propagation, the wavelength and thus the wave number k do not correspond to the actual phase velocity.

Therefore, in this study, based on the definition of the phase velocity, the distance Δx between two consecutively obtained phase distributions is determined. For this, the phase distribution $\theta(x;t)$ at a time t is compared with the shifted phase distribution $\theta(x+\Delta x;t-\Delta T)$ obtained at a time $t-\Delta T$.

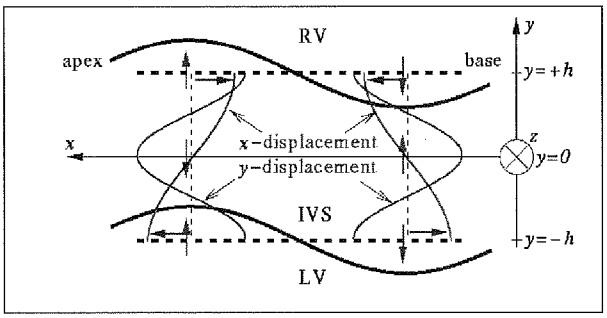

Figure 3. Lamb wave with asymmetric mode of plate waves in the viscoelastic plate with thickness $2h$. The SV-wave component (y-displacement) and longitudinal component (x-displacement) are coupled, and the Lamb wave then propagates along the x-direction.

Regarding the phenomenon of the wave propagation along the viscoelastic plate with thickness $2h$, there are three kinds of plate wave. In the parasternal longitudinal-axis view, the direction ($-y$) of each ultrasonic beam is almost perpendicular to the IVS, and the detected motion is along each beam (y-direction in **Fig. 3**). The pulsive wave propagates along the IVS (x-direction). The vibrations at the RV-side and those at the LV-side are almost parallel (asymmetric). The wavelength λ is about 100 mm for the 30-Hz component and 40-65 mm for

the 90-Hz component. The thickness $2h$ of the IVS is about 10 mm in healthy adults. Thus, the thickness is sufficiently thin. The separate *in vivo* experiments show that the longitudinal component with x-displacement also propagates along the IVS (x-direction). The propagation speed of the shear component is seen to be close to that of the longitudinal component. Thus, there is a likelihood of coupling between the SV-component and the longitudinal component. Given these facts, the detected vibration signal can be modeled by a *Lamb wave with asymmetric mode* in **Fig. 3**.

For the IVS, the blood in RV and LV should be considered. Thus, the model of the *Lamb wave propagating along the viscoelastic plate immersed in blood*, is employed in the present study. Let us define the wave number of the Lamb wave by k_L. By referring to [5], the function, termed $f(k_L,k_p,k_s)$, which should be zero, is given by

$$\begin{aligned} f(k_l,k_p,k_s) &= 4k_l^2\eta\beta\cosh(\eta h)\sinh(\beta h) \\ &\quad -2(k_l^2-k_s^2)^2\sinh(\eta h)\cosh(\beta h) \\ &\quad -\frac{\rho_b\eta k_s^4}{\rho_m\eta_b}\cosh(\eta h)\cosh(\beta h) \\ &= 0 \qquad \cdots\cdots(1) \end{aligned}$$

where k_p and k_s are the wave numbers of the primary wave and the secondary wave, respectively. Using the wave number k_b in blood, $\eta=(k_L^2-k_p^2)^{0.5}$, $\beta=(k_L^2-k_s^2)^{0.5}$, and $\eta_b=(k_L^2-k_b^2)^{0.5}$. ρ_m and ρ_b are the myocardium density and the blood density, respectively, and ρ_m can be approximated by $\rho_b=1.1\times10^3$ kg/m^3. The thickness $2h$ of the IVS is determined from the B-mode image.

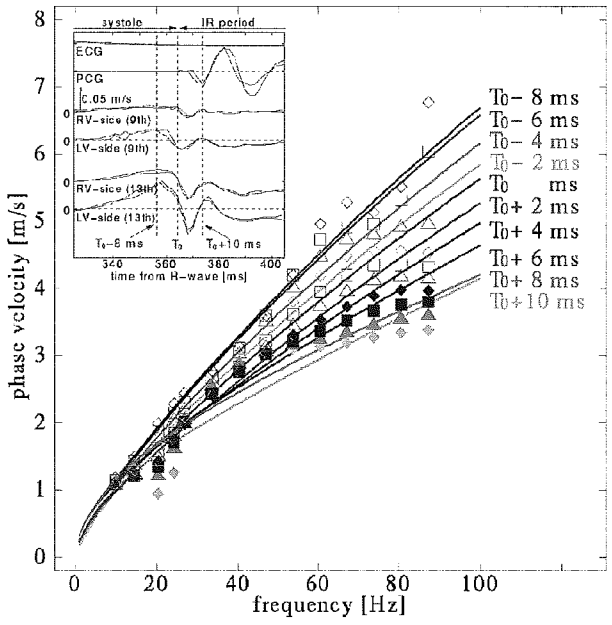

Figure 4. Measured instantaneous phase velocity values c_{phase} and fitted theoretical curves $c_L(\mu,f)$ for the frequency components from 10 Hz to 90 Hz during the period from T_0-8 ms to T_0+10 ms in left upper figure.

By introducing a single Voigt dash-pot model in the frequency range up to 90 Hz, the Lamé elastic constants λ and μ become complex values as $\lambda=\lambda_1-j\omega\lambda_2$ and $\mu=\mu_1+j\omega\mu_2$, respectively [6]. Since λ is about 10^3 times larger than μ for soft tissue due to non-compressibility [6], k_p is approximated by k_b. Since k_L is close to k_s, $\eta\approx k_L$ and $\eta_b\approx k_L$. Therefore, $f(k_L, k_p, k_s)$ of Eq. (1) is approximated by

$$\begin{aligned} f'(c_l,\mu,\omega) &= 4k_l^3\beta\cosh(k_l h)\sinh(\beta h) \\ &\quad -2(k_l^2-k_s^2)^2\sinh(k_l h)\cosh(\beta h) \\ &\quad -k_s^4\cosh(k_l h)\cosh(\beta h) \\ &= 0 \qquad \cdots\cdots(2) \end{aligned}$$

where $k_L=\omega/c_L(\mu,\omega)$ and $k_s=\omega(\rho_m/\mu)^{0.5}$. Thus, $f(c_L,\mu,\omega)$ depends on both the phase velocity $c_L(\mu,\omega)$ of the Lamb wave and the Lamé elastic constant $\mu=\mu_1+j\omega\mu_2$, that is, the elasticity μ_1 and the viscosity μ_2 are estimated so that the theoretical value of the phase velocity $c_L(\mu,\omega)$ of the Lamb wave is to be close to the measured the dispersion of the phase velocity $c_{phase}(\omega)$.

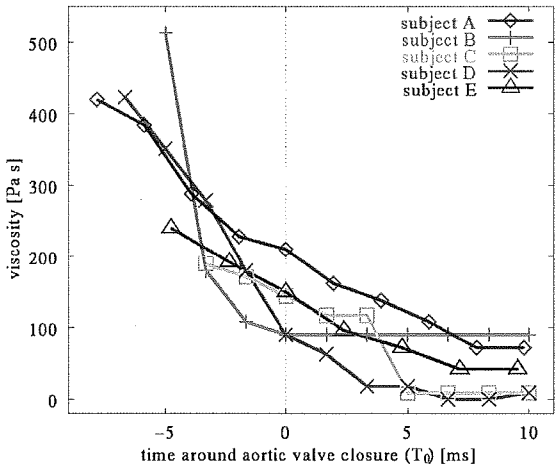

Figure 5. Transient of the viscosity parameters μ_2 measured during the period from T_0-8 ms to T_0+10 ms for five healthy young male subjects.

IV. *In Vivo* Experimental Results

For subject A, by analyzing the period from T_0-8 ms to T_0+10 ms for each frequency component from 10 Hz to 90 Hz, the instantaneous phase velocity $c_{phase}(\omega)$ was obtained as in **Fig. 4**. There is large dispersion among the instantaneous phase velocities $c_{phase}(\omega)$, and they rapidly decrease for all frequency components in this short period around the time of AVC (T_0).

The estimated elasticity μ_1 is about 24-30 kPa and does not change around the time of AVC. The instantaneous viscosity μ_2 of the myocardium rapidly decreases from about 400 Pa•s to 70 Pa•s. This would be due to the rapid decrease in the LV inner pressure from about 120 mmHg to several mmHg, which is caused by relaxation of the myocardium.

For the other four subjects, B-E, the same measurement and analysis were applied, and similar transient characteristics of the viscosity were obtained as shown in **Fig. 5**.

Using the estimated Lamé constant μ, the phase velocity $c_L(\mu, f)$ is obtained. The results are shown by the solid lines in **Fig. 4** for each time t. The estimates $c_L(\mu, f)$ well fit the measured dispersion characteristics $c_{phase}(f)$.

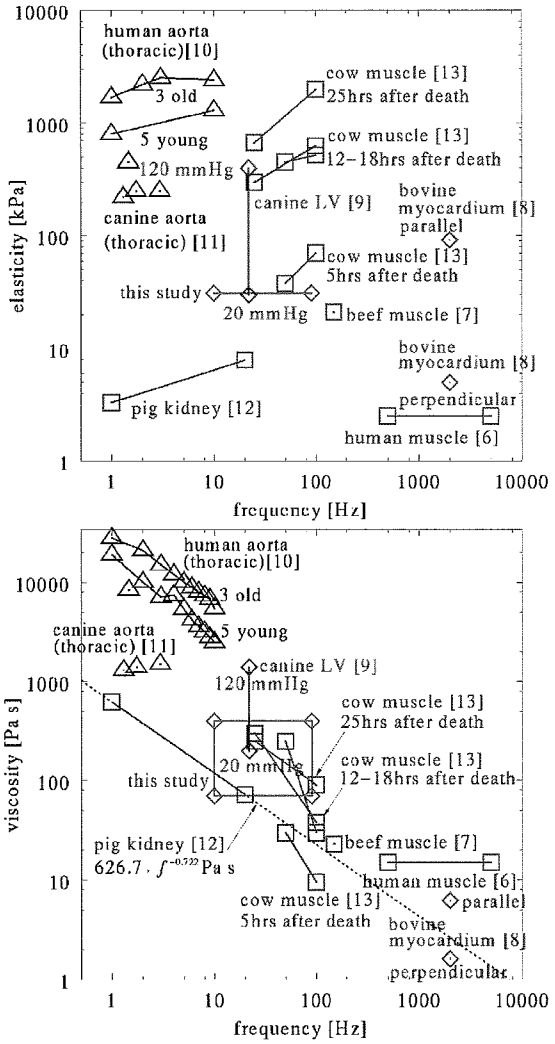

Figure 6. The elastic values $\{\mu_1\}$ and viscosity values $\{\mu_2\}$ reported for the myocardium and soft tissues in the literature using audio or lower frequency components up to 10 kHz.

V. Discussion

The elastic values and viscosity values obtained in the present study are compared with those reported for the myocardium and soft tissues in the literature using audio or lower frequency components up to 10 kHz as shown in **Fig. 6**. Except for those of the present study, all data were measured in *in vitro* experiments. Roughly speaking, the elasticity is large for very low frequency less than 10 Hz and for frequency higher than 1 MHz. In [12], the experimental results for pig kidney showed that the elasticity increases with frequency in the frequency range from 0.01 Hz to 20 Hz. The viscosity data are well fitted to $\eta_2=626.7\times f^{-0.722}$ [Pa•s], which shows that the viscosity decreases with the increase in frequency f. By considering the frequency dependency and the freshness of the specimen in **Fig. 6**, the elasticity and viscosity measured in the present study are close to those measured for the same frequency range in the literature.

VI. Conclusions

We measured rapid and minute vibrations simultaneously at multiple points in the IVS. Clear propagation of the pulsive wave along the IVS was recognized. From the dispersion of the phase velocities, the myocardial viscoelasticity was determined noninvasively for the first time. This method offers potential for *in vivo* imaging of the spatial distribution of the passive mechanical properties of the myocardium and its rapid change during the IR period, which would enable direct assessment of diastolic properties based on myocardial relaxation in heart failure.

Acknowledgment

The author is grateful to Prof. Emeritus Motonao Tanaka of Tohoku University, Prof. Floyd Dunn of the Bioacoustics Research Laboratory of the University of Illinois, Dr. Yoshifumi Saijo of Tohoku University, and Dr. Jens E. Wilhjelm of the Technical University of Denmark for useful discussions. The author also acknowledges the experimental contributions of Dr. Hideyuki Hasegawa in our laboratory.

References

[1] Sutherland G. R., Salvo G. D., Claus P., D'hooge J., Bijnens B. (2004): 'Strain and strain rate imaging: a new clinical approach to quantifying regional myocardial function', *J. Am. Soc. Echocardiogr.*, **17**, pp. 788-802.

[2] Kanai H., Sato M., Koiwa Y., Chubachi N. (1996): 'Transcutaneous measurement and spectrum analysis of heart wall vibrations', *IEEE Trans. Ultrason., Ferroelect., Freq. Contr.*, **43**, pp. 791-810.

[3] Kanai H., Koiwa Y. (2001): 'Myocardial rapid velocity distribution', *Ultrasound Med. Biol.*, **27**, pp. 481-498.

[4] H. Kanai (2004): 'Viscoelasticity Measurement of Heart Wall in *in vivo*', 2004 IEEE International Ultrason. Sympo. Proc., pp. 482-485.

[5] Kundo T. (2003): 'Ultrasonic Nondestructive Evaluation', (CRC Press, New York). Chapters 1 and 4.

[6] Oestreicher H. L. (1951): 'Field and impedance of an oscillating sphere in a viscoelastic medium with an application to biophysics', *J. Acoust. Soc. Am.*, **23**, pp. 707-714.

[7] Catheline S., Wu F., Fink M. (1999): 'A solution to diffraction biases in sonoelasticity: The acoustic impulse technique', *J. Acoust. Soc. Am.*, **105**, pp. 2941-2950.

[8] Choi P.-K., Takahashi H., Onodera Y. (2001): 'Determination of shear elasticity of fibrous soft tissues using surface waves', *The IEICE Transactions*, **J84-A**, pp. 1439-1443. (in Japanese)

[9] Templeton G. H., Nardizzi L. R. (1974): 'Elastic and viscous stiffness of the canine left ventricle', *J. Appl. Physiol.*, **36**, pp. 123-127.

[10] Learoyd B. M., Taylor M. G. (1966): 'Alterations with age in the viscoelastic properties of human arterial walls', *Circ. Res.*, **18**, pp. 278-292.

[11] Gow B. S., Taylor M. G. (1968): 'Measurement of viscoelastic properties of arteries in the living dog', *Circ. Res.*, **23**, pp. 111-122.

[12] Nasseri S., Bilston L. E., Phan-Thien N. (2002): 'Viscoelastic properties of pig kidney in shear, experimental results and modelling', *Rheol. Acta*, **41**, pp. 180-192.

[13] Fitzgerald E. R., Ackerman E., Fitzgerald J. W. (1957): 'Preliminary measurement of the viscoelastic properties of animal tissues at audiofrequencies', *J. Acoust. Soc. Am.*, **29**, pp. 61-64.

Measurement of Myocardial Strain Rate at High Temporal Resolution

Hiroki Yoshiara, Hideyuki Hasegawa, and Hiroshi Kanai
Department of Electronic Engineering
Graduate School of Engineering , Tohoku University
Sendai 980-8579, Japan

***Abstract*—In recent years, there are many studies on measurement of myocardial strain or strain rate, and techniques for measuring them have been developed. However, noninvasive and transmural diagnosis of local myocardial function at high temporal resolution is desired to be established. In this study, five ultrasonic beams were scanned sparsely so that myocardial velocity could be measured at high temporal resolution to calculate strain rate, realizing a frame rate of 630 Hz.**

Keywords-Myocardial contraction/relaxation, Strain rate, Phased tracking method, Frame rate, In vivo experiments.

I. INTRODUCTION

Strain and strain rate imaging have been shown to be useful techniques for assessment of regional myocardial function. It is important to improve both temporal and spatial resolution in measurement of strain rate. In conventional echocardiography, however, we can see mainly shapes of organs and their slow motion with large amplitude. In this case, frame rate is at most 50 Hz, which corresponds to the sampling period of 20 ms.

For noninvasive measurement of the heart wall, other techniques such as Tissue Doppler Imaging (TDI) have been developed. The tissue Doppler imaging (TDI) technique enables determination of the motion distribution in the myocardium in real time. In this method, however, the sampling frequency of the motion of the heart wall is limited to be 200 Hz [1], corresponding to the sampling period of 5 ms. In this study, five ultrasonic beams were scanned sparsely so that myocardial velocity could be measured in wide area at high temporal resolution, realizing a frame rate of 630 Hz.

To improve the spatial resolution, Kanai *et al.* proposed the *phased tracking method* which enables detection of small velocity signals in the heart wall [2]. This method is applied to multiple points preset in the left ventricular (LV) wall along the ultrasonic beam so that the spatial distributions of velocity at those points are simultaneously obtained [3]. In this study, the *phased tracking method* was applied to the points, which were assigned along the ultrasonic beam with smaller intervals in comparison with the previous study [3], to obtain more continuous distribution of myocardial strain rate along the ultrasonic beam.

II. PRINCIPLE

A. Measurement of strain rate by phased tracking method

As illustrated in Fig. 1, both interventricular septum (IVS) and posterior wall were measured. At first, RF data were acquired using a 3.75 MHz sector-type probe of ultrasound diagnostic equipment (ALOKA SSD-6500). The sampling frequency of RF signal was 15 MHz. Secondly, a layer with a thickness of 821 μm was assigned at the surface of the right ventricular (RV) side. The thickness of 821 μm was determined by the duration of an ultrasonic pulse transmitted from the probe. Then, the *phased tracking method* was applied to both top and bottom points of the layer to estimate velocities of these points. Then, the layer was shifted from the right ventricular side to the left ventricular side with intervals of 200 μm along the ultrasonic beam.

We introduced strain rate to evaluate how the thickness of each layer changes with respect to time. Strain rate of the i-th (i=0, 1, 2, ..., N) layer from the RV surface (i=0) is given as follows:

$$S_i(t)=\frac{v(x_{2i};t)-v(x_{1i};t)}{\left|x_{2i}(t)-x_{1i}(t)\right|}, \tag{1}$$

where x_{1i} and x_{2i} are the depths of top and bottom of the i-th layer, respectively. The numerator is the difference between velocities of the top and bottom points, and the denominator is the thickness of the layer for normalization of the velocity defference. Then, strain rate is superimposed on the M-mode image using a color code. Blue means thickening layer which is caused by myocardial contraction, and red means thinning layer which is caused by myocardial relaxation. From a strain rate image superimposed on the M-mode image, we can see how myocardium contracts or relaxes at a certain time at a certain depth.

B. Time interval for analysis

Motion of the heart wall has not only the component parallel to the ultrasonic beam but also has the lateral component perpendicular to ultrasonic beam. Therefore, during a long period such like an entire heart cycle, a point of interest in the wall slips off the ultrasonic beam due to lateral motion.

To overcome this problem, it is necessary to consider appropriate time interval for analysis.

In this report, we investigate a period around the R-wave in electrocardiogram (ECG) and a period around the second heart sound of phonocardiogram (PCG). These intervals correspond to the transient phase from relaxation to contraction, and that from contraction to relaxation, respectively. However, there is a large lateral motion around the second heart sound [4]. The average lateral velocity of about 15 mm/s in this period and the ultrasonic beam width of 2.5 mm at half maximum of sound pressure gives 160 ms in which a point of interest can be in the focal area of the same ultrasonic beam. Therefore, the strain rate was obtained during 160 ms for each period.

III. *In Vivo* Experimental Results

The *phased tracking method* was applied to detection of velocity signals in the IVS and the posterior wall of a healthy 22-year-old male volunteer for the estimation of strain rate. Analyses were conducted along each ultrasonic beam in short time interval around the R-wave in ECG and the second heart sound in PCG.

A. Result around the R-wave

A strain rate distribution around the R-wave was obtained by analyzing ±160 ms around the R-wave. Figure 2 shows the results for the interval around the R-wave. Figure. 2(a) shows strain rate, $\{S_i(t)\}$, defined by Eq. (1). Values of $\{S_i(t)\}$ were color coded according to the coloring scheme on the left-hand side of Fig. 2(a) and superimposed on the M-mode image, where blue means contraction and red means relaxation. Figures. 2(b) and (c) show the ECG and PCG, respectively. Figures. 2(d) and (e) show superimposed estimates of the velocity signals of multiple points in the IVS and posterior wall, respectively. At the beginning of the contraction after the R-wave, the contraction of the RV side precedes that of the LV side by about 35 ms in the IVS, and the endocardium contraction precedes the epicardium contraction by about 20 ms in the posterior wall.

B. Result around the second heart sound

Figure 3 shows the results for the period of ±160 ms around the second heart sound. Measured strain rate, etc. are shown in Figs. 3(a)-(e) as well as Fig. 2. By strain rate image superimposed on the M-mode image shown in Fig. 3(a), it is recognized that the relaxation of the RV side precedes that of the LV side by about 10 ms in IVS, and the relaxation of the epicardium precedes that of the endcardium by about 130 ms in the posterior wall at the beginning of relaxation.

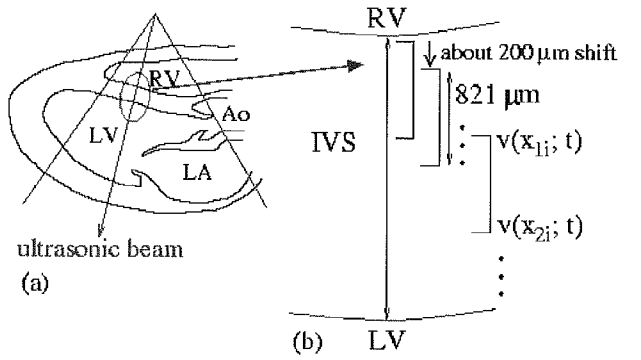

Figure 1: Principle of measurement of strain rate distribution by shifting a layer. (a) Long-axis view of left ventricle. (b) Method of shifting of a layer

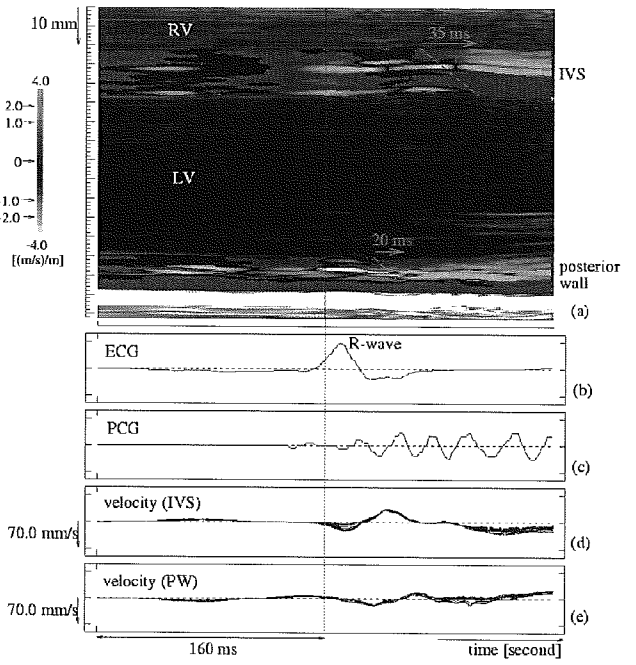

Figure 2: Results around the R-wave. (a) Strain rate, $S_i(t)$, superimposed on the M-mode image. (b) ECG. (c) PCG. (d) Superimposed estimates of the velocity signals of multiple points in IVS. (e) Superimposed estimates of the velocity signals of multiple points in the posterior wall.

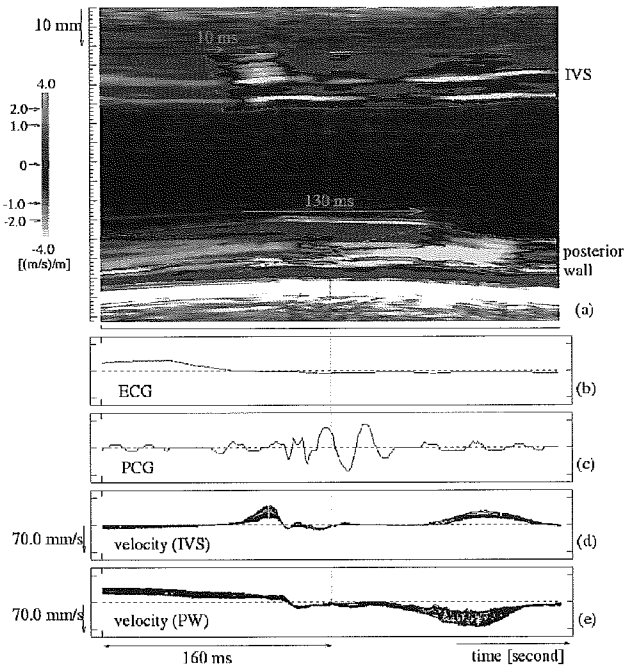

Figure 3: Results around the second heart sound. (a) Strain rate, $S_i(t)$, superimposed on the M-mode image. (b) ECG. (c) PCG. (d) Superimposed estimates of the velocity signals of multiple points in IVS. (e) Superimposed estimates of the velocity signals of multiple points in posterior wall.

C. *Two-dimensional distribution of strain rate around the R-wave*

After the strain rate distribution was estimated along each ultrasonic beam, the estimated strain rates were superimposed on the corresponding region in the B-mode image at every 1.6 ms during the period of $\pm$160 ms. Then, a sequence of these strain rate images was arranged to make a movie of two-dimensional distribution of strain rates. From the movie for the period around the R-wave, it was found that the myocardial contraction and relaxation were in the transition from the base side to the apex side in the IVS. The key frames which show the transition are abstracted and shown in Fig. 4.

D. *Two-dimensional distribution of strain rate around the second heart sound*

A two-dimensional movie for the time around the second heart sound was obtained as well as that around the R-wave. From the movie, it was found that the relaxation was in the transition from the base side to the apex side in the IVS, and from the apex side to the base side in the posterior wall, respectively. However, transition properties in the posterior wall were complicated and further study is needed. The key frames are shown in Fig. 5.

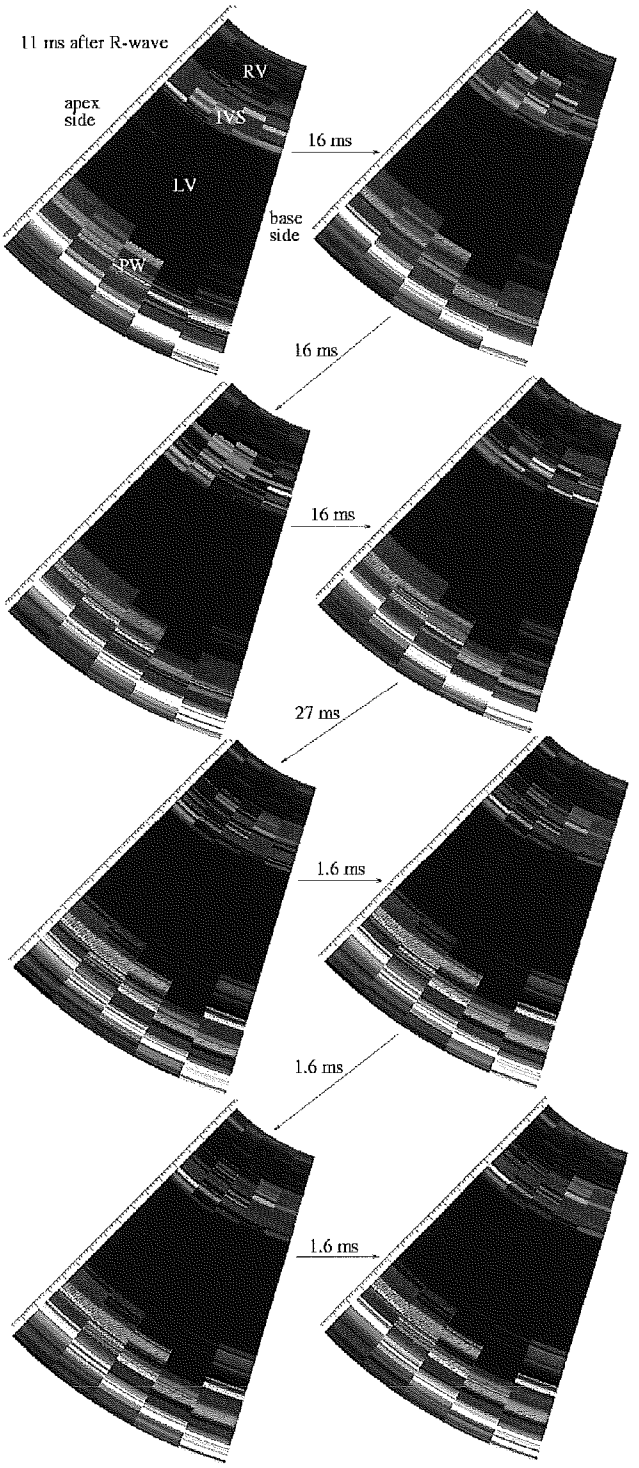

Figure 4: Two-dimensional distribution of strain rate around the R-wave.